FULL PAPER

Metasurfaces

ADVANCED
FUNCTIONAL
MATERIALS

www.afm-journal.de

Plasmonic Metasurfaces for Simultaneous Thermal Infrared Invisibility and Holographic Illusion

Xin Xie, Xiong Li, Mingbo Pu, Xiaoliang Ma, Kaipeng Liu, Yinghui Guo, and Xiangang Luo*

In 1860s, Gustav Kirchhoff proposed his famous law of thermal radiation, setting a fundamental contradiction between the infrared reflection and thermal radiation. Here, for the first time an ultrathin plasmonic metasurface is proposed to simultaneously produce ultralow specular reflection and infrared emission across a broad spectrum and wide incident angle range by combining the low emission nature of metal and the photonic spin–orbit interaction in spatially inhomogeneous structures. As a proof-of-concept, a phase gradient metasurface composed of sub-wavelength metal gratings is designed and experimentally characterized in the infrared atmosphere window of 8–14 µm, demonstrating an ultralow specular reflectivity and infrared emissivity below 0.1. Furthermore, it is demonstrated that infrared illusion could be generated by the metasurface, enabling not only invisibility for thermal and laser detection, but also multifunctionalities for potential applications. This technology is also scalable across a wide range of electromagnetic spectrum and provides a feasible alternative for surface coating.

1. Introduction

According to the Kirchhoff's law[1] and principle of conservation of energy, the relationship between the infrared emissivity (E), absorptivity (A), and reflectivity (R) of nontransparent material can be expressed as $E = A = 1 - R$. Thus materials with low infrared reflectivity generally have high absorptivity and infrared emissivity, and vice versa. It seems impossible to find a material with simultaneous low infrared reflectivity and emissivity, though it is constantly pursued in many technologies including the laser-infrared compatible stealth.[2]

Recent development of metasurfaces pointed out conceptually new methods to manipulate the electromagnetic waves. In short, the metasurface is composed of artificial atoms that locally tailor the surface electromagnetic response at the sub-wavelength scale accompanied by dramatic light confinement.[3–5] A variety of unique phenomena and applications based on metasurfaces have been demonstrated—for example, abnormal near-field interference,[6] vortex beam generation,[7–10] polarization manipulation,[11–17] flat lenses,[18–21] spin-Hall effect of light,[22–24] optical holography,[25–28] and perfect absorption.[29–31] On the basis of this local phase and amplitude control capability, various metasurfaces have been put forward and experimentally characterized to reduce the reflection and scattering of objects. For instance, ultrathin metasurface absorbers can reduce the reflectance by absorbing the incident light energy.[29,32] To realize compatibility of thermal infrared invisibility and laser cross section reduction, narrowband absorbers working at infrared laser wavelengths are required. Although this technique could reduce the thermal emission to some extent, the performance is still far from ideal and not easy to be further improved.[33] Another promising approach is using phase gradient metasurfaces to guide backscattered waves to other directions, resulting in a remarkable reduction or increase of specular reflectivity.[34–36] However, most current phase-gradient metasurfaces cannot achieve thermal invisibility due to the high infrared absorption/emission arising from the complex metal-dielectric structures (some dielectrics such as silicon, germanium are nearly free of loss in the infrared spectrum but fragile; others such as most polymers are flexible but highly lossy).

In this paper, we propose and experimentally demonstrate an all-metallic scheme to simultaneously reduce the specular reflection and infrared emission in broad wavebands and wide incident angles, by combining the low emission nature of plasmonic metal and geometric phase originated from spin–orbit interaction in space-variant anisotropic material.[37,38] Additional advantages of these all-metallic structures are their good mechanical properties, such as the high strength, large flexibility, and good ductility, which are essential to engineering applications. We also design and experimentally characterized a high performance reflective meta-hologram, proving that these metasurfaces also have the potential to act as multifunctional reflective optical components.

Dr. X. Xie, Prof. X. Li, Prof. M. Pu, Prof. X. Ma, Dr. K. Liu, Dr. Y. Guo, Prof. X. Luo
State Key Laboratory of Optical Technologies on Nano-Fabrication and Micro-Engineering
Institute of Optics and Electronics
Chinese Academy of Sciences
Chengdu 610209, China
E-mail: lxg@ioe.ac.cn
Dr. X. Xie, Prof. X. Li, Prof. M. Pu, Prof. X. Ma, Prof. X. Luo
University of Chinese Academy of Sciences
Beijing 100049, China

The ORCID identification number(s) for the author(s) of this article can be found under https://doi.org/10.1002/adfm.201706673.
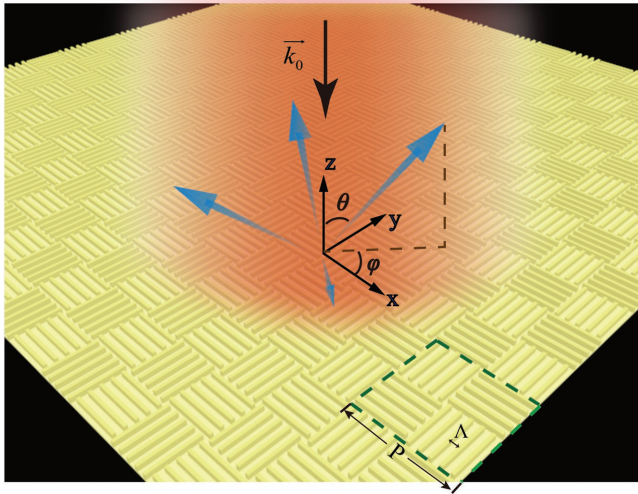
Figure 1. Schematic of the all-metallic metasurface, showing the electromagnetic scattering in the upper half-space. The dashed box indicates the super cell of the metasurface.

2. Results

According to the spin–orbit interaction in inhomogeneous structures, under circularly polarized light illumination, the anisotropic reflection would result in a geometric phase for the cross-polarized light, which is twice the orientation angle of the metallic strips (ζ) and can be written as $\Phi = 2\sigma\zeta$,[8,39] where $\sigma = \pm 1$ denotes the left-handed circular polarization and right-handed circular polarization. By designing the phase distribution, the reflected beam will be forced to propagate in well-defined ways with respect to the specular reflection direction.[34] According to this principle, our designed metasurface, consisting of a chessboard-like configuration of orthogonal metallic gratings (**Figure 1**), will induce a relative phase change of $\Delta\Phi = \pi$. In this circumstance, the metasurface will be virtually shaped just like a chessboard pattern with different heights.[40] Under normal incidence, the backscattered energy is redirected to four diagonal directions where $\varphi = 45°$, $135°$, $225°$, and $315°$, thus the reflected wave along the specular direction is cancelled out, as shown in Figure 1. The angle between each beam with the z-axis can be calculated by[22]

$$\theta = \arcsin\left(\frac{\lambda}{P}\right) \tag{1}$$

where λ is the wavelength of incident wave, P is the pixel size of the metasurface satisfying $P = 2n\Lambda$, Λ is the grating period, and n is the number of metallic strips. Due to its fourfold geometrical symmetry, the metasurface not only performs well for circularly polarized incidence, but also for linearly polarized incidence because it can be decomposed into two circularly polarized incidences with opposite handedness but same amplitude.[34]
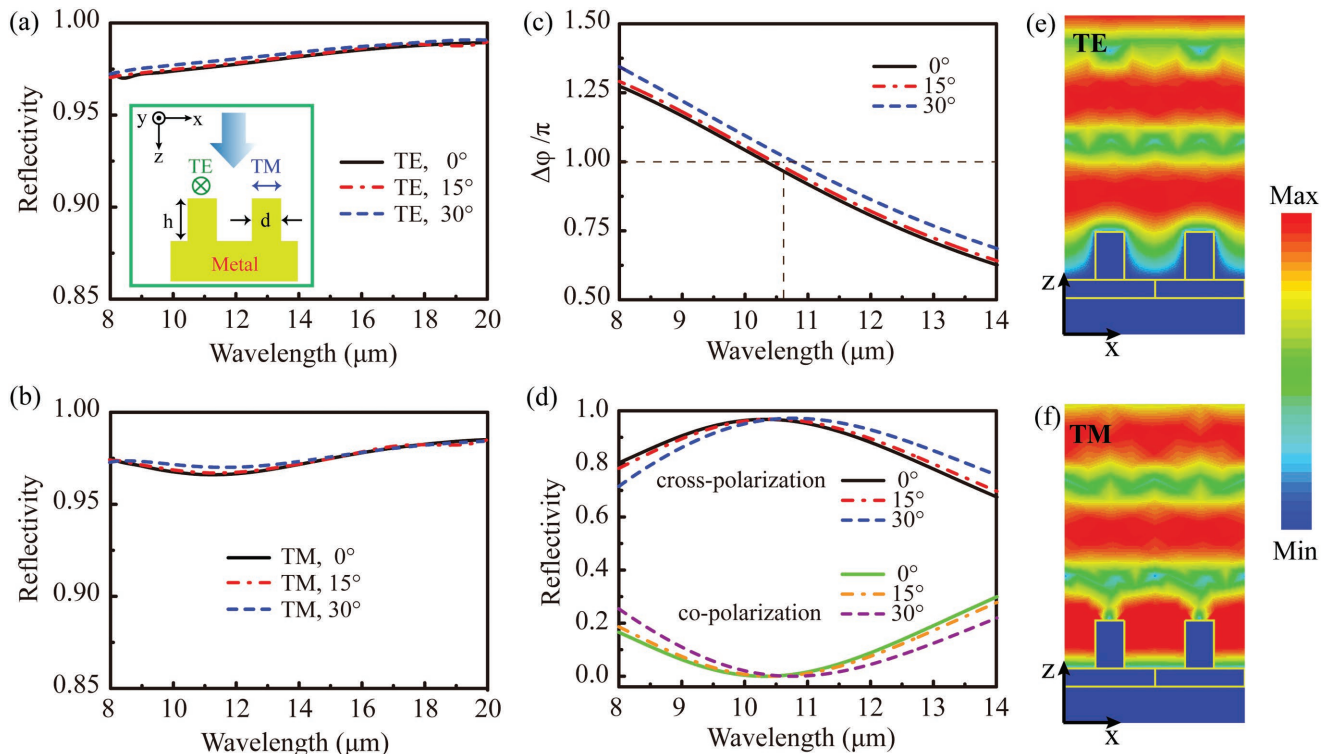
Figure 2. a,b) Simulated reflectivities of the unit cell under TE and TM polarized illumination for different incident angles. The inset in (a) illustrates the geometry of the element array. c) Relative phase differences between x and y polarizations for different incident angles. d) Simulated reflectivities for cross-polarization and copolarization under circularly polarized illumination for different incident angles. e,f) Simulated optical field |E| distributions of the gratings under TE and TM polarizations for normal incidence at 10.6 µm.

**ADVANCED
SCIENCE NEWS**
www.advancedsciencenews.com

**ADVANCED
FUNCTIONAL
MATERIALS**
www.afm-journal.de

To better understand the electromagnetic properties of the basic elements and gain more physical insights into the underlying mechanism of the metasurface, numerical simulations are performed with commercial software CST Microwave Studio. Unit cell boundary is used in the simulation to take the mutual coupling of adjacent elements into account. For transverse electric (TE) and transverse magnetic (TM) polarized incidence, the reflectivities for different incident angles are calculated, as shown in **Figure 2**a,b. The corresponding geometric parameters are optimized as $\Lambda = 5$ µm, $d = 1.6$ µm, $h = 2.7$ µm, where d is the width and h is the thickness of each gold strip (see the inset in Figure 2a). It is clearly observed that the reflectivity is more than 95% at the wavelength beyond 8 µm for all the incident cases, indicating the metallic gratings possess ultralow absorption loss and infrared emissivity.

In the following, we focus on the polarization conversion effect of the all-metallic grating. Figure 2c shows the relative phase differences between the x (TM) and y (TE) polarized components ($\Delta \Phi = \Phi_x - \Phi_y$) for different incident angles. One can see that the phase shift at the wavelength of 10.6 µm is about π, thus the corresponding conversion efficiency is up to nearly 100%. The cross-polarized and copolarized reflectivities under circularly polarized illumination for different incident angles are calculated, as shown in Figure 2d. According to the generalized Snell's law,[37,41] the copolarized component corresponds to the specular reflectivity which means the reflected wave will propagate in accordance with the traditional reflection law, while the cross-polarized component corresponds to the reflected wave that will be steered to predesigned directions. We observe that the copolarized reflectivities are less than 0.1 from 8.5 to 12.5 µm and the minimum reflection (nearly 0) occurs at about 10.6 µm. Although the wavelength for minimum reflectivity is slightly shifted toward a larger value when increasing the oblique incident angle, the mean values of the copolarized reflectivity are rather small in the whole infrared window of 8–14 µm. Figure 2e,f shows the simulated optical field |E| distributions of the gratings under TE and TM polarizations at the wavelength of 10.6 µm, where strong reflections are clearly presented. The two orthogonal waves are reflected at different interfaces. The TE polarized light cannot penetrate into the grating and reflects at the top surface of the structure due to the sub-wavelength scale of the metallic grating, while

the TM polarized light reflects at the bottom of the structure, resulting in the phase differences between the reflected TE and TM components.

Subsequently, full-wave simulations are performed to validate the performance of the designed metasurface. A subgroup made of 2×2 gratings with orthogonal orientations (dashed box in Figure 1) is used in the simulation with periodic boundaries. Every grating is comprised of five identical metallic strips ($n = 5$) to increase the geometrical similarity for each element, which complies with the unit cell boundary hypothesis in previous simulation. In fact, since the subgroup could be optimized rigorously, the final details of the structure model may be different from the original unit cells, especially for limited numbers of stripes. In order to verify the polarization-independent property, both TM and TE-polarized plane waves are considered to illuminate on the structure at normal incidence. As we expected, the calculated reflectivities under the two polarization illuminates are identical, as shown in **Figure 3**a. In comparison, an unpatterned gold plate with the same dimensions corresponding to the metasurface is simulated. It is obvious that the specular reflectivity for the metasurface is dramatically smaller than the metal. The reflectivity at 8.5–12.5 µm is less than 0.1 and the minimum value occurs at about 10.6 µm. The scattering patterns of the metasurface and the metallic plate for normal incidence at 10.6 µm are also compared in Figure 3b–e. From Figure 3c,e, we observe highly directed specular reflection for the metallic plate. However, when the metallic plate is covered by subwavelength gratings, the reflected energy is mainly split into four diagonal directions in the 45° planes ($\varphi = 45°$ and 135°), resulting in significant reduction of reflection in the normal direction, as shown in Figure 3b. The scattering pattern of the metasurface at $\varphi = 45°$ (or 135°) plane is presented in Figure 3d, from which one can see that the scattering angle θ is about 12.5°, in good agreement with the theoretical calculation (12.2°) with Equation (1). Note that the scattering angle can be designed to be larger by reducing the number of metallic strips (n). From Figure 3d, one can find that the scattering amplitude of each beam is ≈0.25 (1/4) of the incident beam, proving that the metasurface can achieve almost full reflection.

Owing to the scalability of Maxwell's Equations, the metallic metasurface can be extended to other electromagnetic spectrum, including visible, near-infrared, and microwave regimes, which
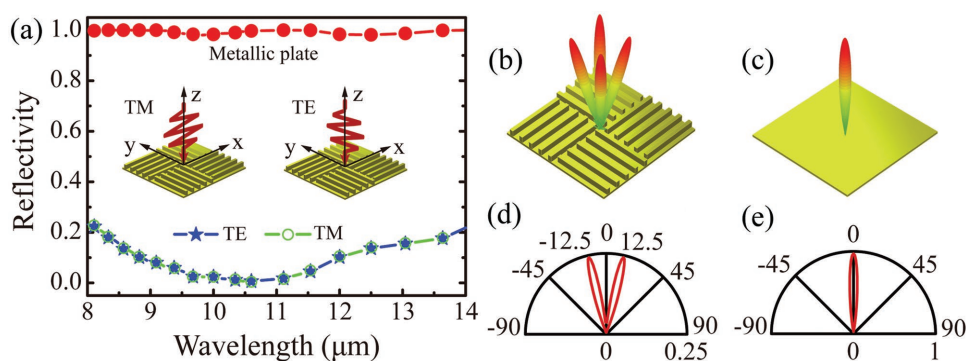

Figure 3. a) Full-wave simulated reflectivities of the metasurface and the metallic plate for TE or TM polarized light at normal incidence. b,c) 3D scattering patterns of the metasurface and the metallic plate for normal incidence at 10.6 µm, respectively. d,e) Scattering patterns at $\varphi = 45°$ plane for the metasurface and the metallic plate.

**ADVANCED
SCIENCE NEWS**
www.advancedsciencenews.com

**ADVANCED
FUNCTIONAL
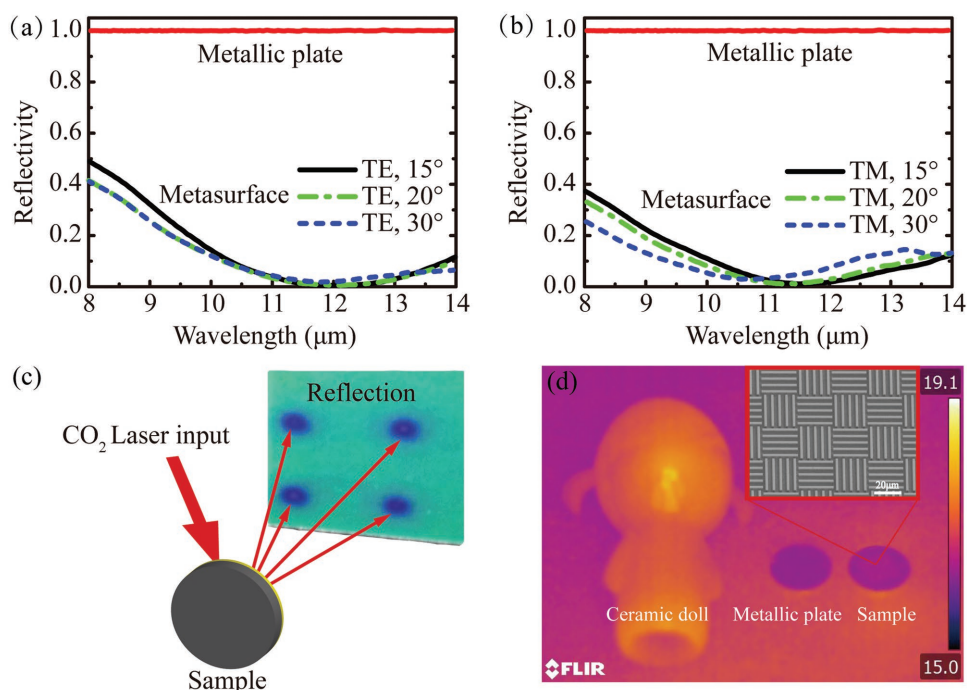MATERIALS**
www.afm-journal.de

Figure 4. a,b) Measured reflectivity of the metasurface under oblique incidences for TE and TM polarization, respectively. c) Measured scattering pattern for the metasurface sample using a CO_2 Laser. d) Thermal infrared image of a ceramic doll, a metallic plate and the fabricated sample. Inset is the scanning electron microscope (SEM) image of the fabricated metasurface. Scale bar: 20 µm.

also exhibit excellent low specular reflection and low infrared emission performance. As shown in Figure S1 (Supporting Information), in near-infrared region, the designed metasurface can achieve a specular reflectivity less than 0.1 at 0.9–1.6 µm, which covers typical laser wavelengths for laser radar. Owing to the plasmonic resonance effect, the relative wavelength band is larger than the previous sample. Simultaneously, the structure exhibits ultralow infrared emissivity at the wavelengths beyond 0.9 µm. Similarly, the multifunctional performance is feasible in microwave regime, as shown in Figure S2 (Supporting Information), where the specular reflectivity from 8 to 16 GHz is suppressed to be less than −10 dB. Compared with traditional metamaterial or metasurfaces absorbers, this design includes only metals thus possesses some unique advantages including much better durability in complex environments, especially when high-temperature-resistant refractory metals are adopted.[37,42]

3. Conclusion

In summary, we have proposed a multifunctional metasurface scheme to achieve ultralow specular reflectivity and thermal infrared emissivity in broad frequency spectrum and wide incidence angles simultaneously. Low emission is resulting from the

all-metallic structures, and low reflection is implemented by tailoring the wave fronts and redirecting the reflected energy to nonthreatening angles. We also demonstrated that any desired wavefront can be reconstructed by more elaborate design of the phase distribution carried by the metasurface. It is also worth mentioning that all-metallic structures have good mechanical and thermal properties for engineering applications involving
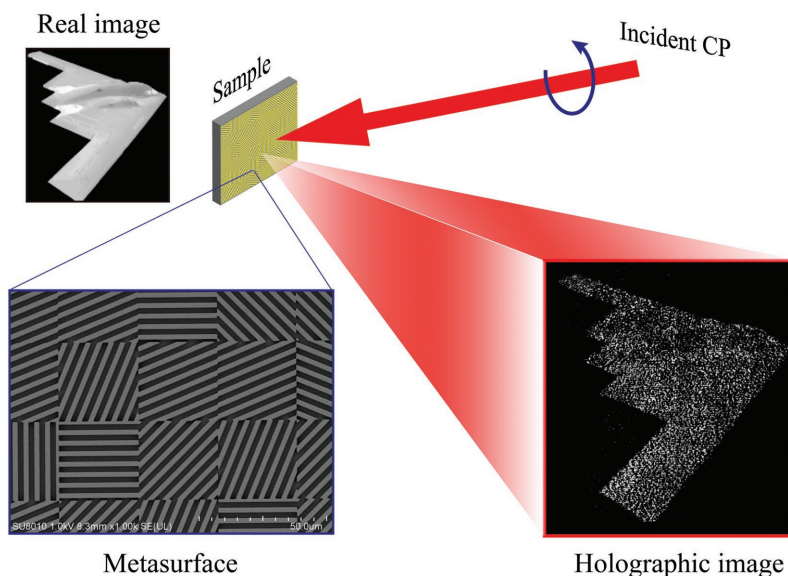

Figure 5. SEM image of the all-metallic metasurface hologram and the measured holographic image at a wavelength of 10.6 µm. The width, period, and thickness of the grating are 1.8, 4, and 2.65 µm. One pixel of the hologram has a size of 30 × 30 µm.

**ADVANCED
SCIENCE NEWS**
www.advancedsciencenews.com

**ADVANCED
FUNCTIONAL
MATERIALS**
www.afm-journal.de

conformal shaping and complex environments. Thus our presented metasurfaces may stimulate the development of multiphysical and multispectral applications as well as high-efficiency and broadband reflective optical elements.

4. Experimental Section

To investigate the simultaneous low reflection and low infrared emission properties experimentally, a metasurface with an area of 12×12 mm^2 using laser direct writing combined with conventional photolithography techniques was fabricated. First, a layer of photoresist AZ1500 was coated on a 1 mm thick quartz substrate and then a 100 nm thick SiO$_2$ film was deposited upon the photoresist layer using magnetron sputtering. Subsequently, a 500 nm thick photoresist AZ1500 was coated on the SiO$_2$ layer. The target pattern was formed by laser direct writing on the upper photoresist layer. Subsequently, the pattern was transferred into the SiO$_2$ film using reactive ion etching with the gas of CHF$_3$. Then changing the etch gas as O$_2$ to transfer the pattern into the photoresist AZ1500. Finally, SiO$_2$ was etched off in the areas where the target patterns locate, and an Au layer with a thickness of 200 nm was sputtered on the disposed photoresist, resulting in the metasurface sample. Although the fabricated metasurface is not an ideal all-metallic structure as simulated, the same optical functionality can still be achieved (see Figure S3 for the detail, Supporting Information).

The reflectivity of the fabricated sample was measured using the Fourier transform infrared spectrometer. A pair of off-axis concave mirrors mounted on two guiding rails and fixed with the emitter and detector, respectively, was used to control the incident and reflected angles. Due to the geometric dimension limit of two concave mirrors, the minimal specular angle can only be adjusted to 15°. Therefore, here three specular angles—15°, 20°, and 30°—for measurements were considered. The measured reflectivities of the metasurface under TE and TM polarized incidences in 8–14 µm are recorded in **Figure 4**a,b, along with a same-sized Au plate without the sub-wavelength gratings. It was observed that the specular reflectivity was less than 0.1 from 10 to 14 µm for all the incidence angles, indicating the metasurface has excellent broadband and wide incidence angles properties in scattering the laser beam.

To check the scattering pattern of the metasurface, a CO$_2$ Laser ($\lambda = 10.6$ µm) was illuminated on the sample with a small oblique angle of ≈10°, the reflection signal was collected with an infrared color plate (Thermochromic Liquid Crystal, VRC6S, Thorlabs). As shown in Figure 4c, four spots were clearly observed on the color plate, indicating the four reflected beams.

The low infrared emission property was characterized by comparing the thermal infrared image of the fabricated sample with a ceramic doll and a metallic plate. The measurement was performed at room temperature (20 °C) using a commercial thermal infrared imager and the results are shown in Figure 4d, where the apparent temperature value is indicated by the color bar. Clearly, the apparent temperature of the ceramic doll is much higher than that of the metallic plate and the metasurface sample, indicating the metasurface has a nearly equal infrared emission as the flat metal plate.

Although our proposed metasurface consists of metallic gratings with only two orthogonal orientation angles, the design can be easily extended to create more complex optical elements. For example, a high-performance metahologram was chosen to demonstrate the superb capability of phase manipulation of the metallic metasurface at the infrared wavelengths. The phase map of a holographic image was computed, the binary B2 stealth aircraft model, by means of the point source algorithm.[25,26] The required phase was coded via the rotation of the birefringent metallic gratings and an eight-level phase gradient metasurface was considered in the experiment. The SEM image of the fabricated sample and the measured results are shown in **Figure 5**, giving a successful demonstration of the full 0–2π phase coverage.

Compared to previous metamaterial and metasurface holograms,[26,43,44] this technique shows obvious advantages such as high efficiency (≈85%), broadband operation, easy-fabrication, and multifunction compatibility. In addition, the high efficiency and broadband properties enable the implementation of many other high performance reflective optical components such as lenses, wave plates, and polarization beam splitters. It is worth noting that, the thermal emission of this metahologram is comparable low to the first sample due to the same metal material is used.

Conflict of Interest

The authors declare no conflict of interest.

[1] J.-J. Greffet, M. Nieto-Vesperinas, *J. Opt. Soc. Am. A* **1998**, *15*, 2735.

[2] C. J. David, *Radar and Laser Cross Section Engineering*, AIAA, Reston, VA, **2005**.

[3] N. Yu, F. Capasso, *Nat. Mater.* **2014**, *13*, 139.

[4] M. Pu, X. Ma, X. Li, Y. Guo, X. Luo, *J. Mater. Chem. C* **2017**, *5*, 4361.

[5] N. Meinzer, W. L. Barnes, I. R. Hooper, *Nat. Photonics* **2014**, *8*, 889.

[6] X. Luo, T. Ishihara, *Appl. Phys. Lett.* **2004**, *84*, 4780.

[7] P. Genevet, N. Yu, F. Aieta, J. Lin, M. A. Kats, R. Blanchard, M. O. Scully, Z. Gaburro, F. Capasso, *Appl. Phys. Lett.* **2012**, *100*, 013101.

[8] M. Pu, X. Li, X. Ma, Y. Wang, Z. Zhao, C. Wang, C. Hu, P. Gao, C. Huang, H. Ren, X. Li, F. Qin, M. Gu, M. Hong, X. Luo, *Sci. Adv.* **2015**, *1*, e1500396.

[9] J. Jin, M. Pu, Y. Wang, X. Li, X. Ma, J. Luo, Z. Zhao, P. Gao, X. Luo, *Adv. Mater. Technol.* **2017**, *2*, 1600201.

[10] J. Zeng, L. Li, X. Yang, J. Gao, *Nano Lett.* **2016**, *16*, 3101.

[11] N. K. Grady, J. E. Heyes, D. R. Chowdhury, Y. Zeng, M. T. Reiten, A. K. Azad, A. J. Taylor, D. A. R. Dalvit, H.-T. Chen, *Science* **2013**, *340*, 1304.

[12] M. Pu, P. Chen, Y. Wang, Z. Zhao, C. Huang, C. Wang, X. Ma, X. Luo, *Appl. Phys. Lett.* **2013**, *102*, 131906.

[13] Y. Guo, Y. Wang, M. Pu, Z. Zhao, X. Wu, X. Ma, C. Wang, L. Yan, X. Luo, *Sci. Rep.* **2015**, *5*, 8434.

[14] Z. Zhang, J. Luo, M. Song, H. Yu, *Appl. Phys. Lett.* **2015**, *107*, 241904.

**ADVANCED
SCIENCE NEWS**

www.advancedsciencenews.com

**ADVANCED
FUNCTIONAL
MATERIALS**

www.afm-journal.de

[15] P. C. Wu, J.-W. Chen, C.-W. Yin, Y.-C. Lai, T. L. Chung, C. Y. Liao, B. H. Chen, K.-W. Lee, C.-J. Chuang, C.-M. Wang, D. P. Tsai, *ACS Photonics* **2018**, https://doi.org/10.1021/acsphotonics.7b01527.

[16] P. C. Wu, W.-Y. Tsai, W. T. Chen, Y.-W. Huang, T.-Y. Chen, J.-W. Chen, C. Y. Liao, C. H. Chu, G. Sun, D. P. Tsai, *Nano Lett.* **2017**, *17*, 445.

[17] P. C. Wu, W. Zhu, Z. X. Shen, P. H. J. Chong, W. Ser, D. P. Tsai, A.-Q. Liu, *Adv. Opt. Mater.* **2017**, *5*, 1600938.

[18] F. Aieta, P. Genevet, M. A. Kats, N. Yu, R. Blanchard, Z. Gaburro, F. Capasso, *Nano Lett.* **2012**, *12*, 4932.

[19] D. Lin, P. Fan, E. Hasman, M. L. Brongersma, *Science* **2014**, *345*, 298.

[20] Y. Li, X. Li, M. Pu, Z. Zhao, X. Ma, Y. Wang, X. Luo, *Sci. Rep.* **2016**, *6*, 19885.

[21] S. Wang, P. C. Wu, V.-C. Su, Y.-C. Lai, C. H. Chu, J.-W. Chen, S.-H. Lu, J. Chen, B. Xu, C.-H. Kuan, T. Li, S. Zhu, D. Tsai, *Nat. Commun.* **2017**, *8*, 187.

[22] X. Luo, M. Pu, X. Li, X. Ma, *Light Sci. Appl.* **2017**, *6*, e16276.

[23] X. Yin, Z. Ye, J. Rho, Y. Wang, X. Zhang, *Science* **2013**, *339*, 1405.

[24] A. Shaltout, J. Liu, A. Kildishev, V. Shalaev, *Optica* **2015**, *2*, 860.

[25] L. Huang, X. Chen, H. Mühlenbernd, H. Zhang, S. Chen, B. Bai, Q. Tan, G. Jin, K.-W. Cheah, C.-W. Qiu, J. Li, T. Zentgraf, S. Zhang, *Nat. Commun.* **2013**, *4*, 2808.

[26] X. Li, L. Chen, Y. Li, X. Zhang, M. Pu, Z. Zhao, X. Ma, Y. Wang, M. Hong, X. Luo, *Sci. Adv.* **2016**, *2*, e1601102.

[27] L. Liu, X. Zhang, Z. Zhao, M. Pu, P. Gao, Y. Luo, J. Jin, C. Wang, X. Luo, *Adv. Opt. Mater.* **2017**, *5*, 1700429.

[28] W. Wan, J. Gao, X. Yang, *ACS Nano* **2016**, *10*, 10671.

[29] Q. Feng, M. Pu, C. Hu, X. Luo, *Opt. Lett.* **2012**, *37*, 2133.

[30] M. Pu, Q. Feng, M. Wang, C. Hu, C. Huang, X. Ma, Z. Zhao, C. Wang, X. Luo, *Opt. Express* **2012**, *20*, 2246.

[31] P. C. Wu, N. Papasimakis, D. P. Tsai, *Phys. Rev. Appl.* **2016**, *6*, 044019.

[32] C. M. Watts, X. Liu, W. J. Padilla, *Adv. Mater.* **2012**, *24*, OP98.

[33] C. Zhang, C. Huang, M. Pu, J. Song, Z. Zhao, X. Wu, X. Luo, *Sci. Rep.* **2017**, *7*, 5652.

[34] M. Pu, Z. Zhao, Y. Wang, X. Li, X. Ma, C. Hu, C. Wang, C. Huang, X. Luo, *Sci. Rep.* **2015**, *5*, 9822.

[35] X. Ni, Z. J. Wong, M. Mrejen, Y. Wang, X. Zhang, *Science* **2015**, *349*, 1310.

[36] Y. Guo, L. Yan, W. Pan, L. Shao, *Sci. Rep.* **2016**, *6*, 30154.

[37] X. Luo, *Sci. China: Phys., Mech. Astron.* **2015**, *58*, 594201.

[38] K. Y. Bliokh, F. J. Rodriguez-Fortuno, F. Nori, A. V. Zayats, *Nat. Photonics* **2015**, *9*, 796.

[39] R. Bhandari, *Phys. Rep.* **1997**, *281*, 1.

[40] S. Simms, V. Fusco, *Electron. Lett.* **2008**, *44*, 316.

[41] N. Yu, P. Genevet, M. A. Kats, F. Aieta, J.-P. Tetienne, F. Capasso, Z. Gaburro, *Science* **2011**, *334*, 333.

[42] W. Li, U. Guler, N. Kinsey, G. V. Naik, A. Boltasseva, J. Guan, V. M. Shalaev, A. V. Kildishev, *Adv. Mater.* **2014**, *26*, 7959.

[43] S. Larouche, Y.-J. Tsai, T. Tyler, N. M. Jokerst, D. R. Smith, *Nat. Mater.* **2012**, *11*, 450.

[44] D. Wen, F. Yue, G. Li, G. Zheng, K. Chan, S. Chen, M. Chen, K. F. Li, P. W. H. Wong, K. W. Cheah, E. Yue Bun Pun, S. Zhang, X. Chen, *Nat. Commun.* **2015**, *6*, 8241.